Sensitivity of CO oxidation toward metal oxidation state in ceria-supported catalysts: an operando DRIFTS-MS study

Andre Kaftan, Fabian Kollhoff, Nguyen Thanh-Son, L. Piccolo, Mathias Laurin, Joerg Libuda

Journal Name

ARTICLE

Sensitivity of CO oxidation toward metal oxidation state in ceria-supported catalysts: an operando DRIFTS-MS study

Received 00th January 20xx,
Accepted 00th January 20xx

DOI: 10.1039/x0xx00000x

www.rsc.org/

Andre Kaftan,[a] Fabian Kollhoff,[a] Thanh-Son Nguyen,[b] Laurent Piccolo,[b] Mathias Laurin,[a] Jörg Libuda[a,c]

The oxidation of carbon monoxide has been studied on pristine CeO_2, Rh-CeO_2, and Pt-CeO_2 powders prepared in one step by solution combustion synthesis (SCS). The reaction was cycled between an oxygen-rich and a CO-rich feed with regard to the stoichiometric conditions. CO_2 production was monitored by mass spectrometry while the surface species were probed by operando DRIFTS (Diffuse Reflection Infrared Fourier Transform Spectroscopy). Whereas the reaction starts above 150 °C on CeO_2 and Rh-CeO_2 and does not depend on the state of the surface (oxidized or reduced), Pt-CeO_2 shows strong dependency on initial state and substantial activity already at much lower temperatures with the CO-rich feed. We relate this result to a change in the oxidation state of Pt in strong interaction with ceria.

Introduction

The rare-earth oxide cerium dioxide is an active phase in numerous heterogeneously catalyzed redox processes.[1-3] Its unique properties can be explained by its ability to rapidly release and store oxygen from the environment, thereby switching the oxidation state of the cation (Ce^{4+} or Ce^{3+}). Associated with a high mobility of the oxygen, the process plays an active role in oxidation reactions such as CO oxidation in three-way catalytic converters[4] or the preferential oxidation of CO in hydrogen excess (PROX), a process to remove CO impurities from reformate hydrogen for fuel cell applications.[5-8]

It was recently shown that metal-ceria powders can be prepared by a one-pot solution combustion synthetic (SCS) route.[9, 10] SCS is a relatively simple and inexpensive method for preparing metal oxides. It consists in the fast and self-sustained combustion of a preheated aqueous solution of a metallic salt and an organic fuel. The solid oxide material obtained is generally nanocrystalline, making it highly attractive for heterogeneous catalysis, in particular for applications requiring a highly stable catalyst.[11-18]

In this paper, we run CO oxidation cycles on pristine ceria, Rh-ceria, and Pt-ceria powders prepared by SCS. CO oxidation is the archetypal reaction to test the catalytic performance of ceria powders. The catalytic conversion to CO_2 was followed by mass spectrometry, and operando diffuse reflectance infrared Fourier transform spectroscopy (DRIFTS) was used to follow the evolution of the adsorbates as well as possible changes at the surface of the powders.

[a] *Lehrstuhl für Physikalische Chemie II, Friedrich-Alexander-Universität Erlangen-Nürnberg, Egerlandstraße 3, 91058 Erlangen, Germany*
[b] *Institut de recherches sur la catalyse et l'environnement de Lyon (IRCELYON), UMR 5256 CNRS and Université Lyon 1, 2 Avenue Albert Einstein, 69626 Villeurbanne, France*
[c] *Erlangen Catalysis Ressource Center and Interdisciplinary Center for Interface-Controlled Processes, Friedrich-Alexander-Universität Erlangen-Nürnberg, 91058 Erlangen, Germany*

Experimental

Sample preparation in one step, one pot solution combustion synthesis

The samples were prepared by solution combustion synthesis (SCS), using ceric ammonium nitrate, CAN [$(NH_4)_2Ce(NO_3)_6$, Sigma-Aldrich, 99.99%] as both ceria precursor salt and oxidizing agent. The Pt and Rh precursors were $H_2PtCl_6.6H_2O$ (Strem Chemicals, 38–40% Pt), and $RhCl_3$ (Sigma-Aldrich, 38–40% Rh), respectively. Glycine ($C_2H_5NO_2$, Sigma-Aldrich, 99%) was used as fuel. The CAN:glycine:metal precursor mixture composition was chosen in order to obtain stoichiometric proportions of oxidizer and fuel (*i.e.*, with the oxidizing/reducing valence ratio of the redox mixture equal to 1)[19] and to reach the desired metal loading (1 wt%).

Practically, a borosilicate beaker (300 cm^3) containing a mixture of CAN (5.00 g), glycine (1.82 g), Pt or Rh precursor, and 30 mL deionized water was introduced into a muffle furnace (Carbolite ELF 11/6) maintained at 350 °C. At the point of complete dehydration (5–10 min), the solution started boiling and foaming, and ignition took place after a few seconds with rapid evolution of a large quantity of gases. This yielded a voluminous solid product within a few minutes. The powder color ranged from pale yellow (CeO_2) to brown-grey (Pt and Rh-CeO_2).

Chlorine residues from the preparation process may have an influence on the catalytic reactivity. In particular, it is known that under certain conditions the chlorination of ceria leads to CeOCl phase formation.[20] Infrared spectroscopy of CO adsorbed on such a phase shows an absorption band at around 2175 cm^{-1},[21] which is not observed in our work. However, in our comparative study the influence of chloride is believed to be of much lesser importance than that of the metal nature since both catalysts were prepared in the same way, using the same types of (chloride) precursors.

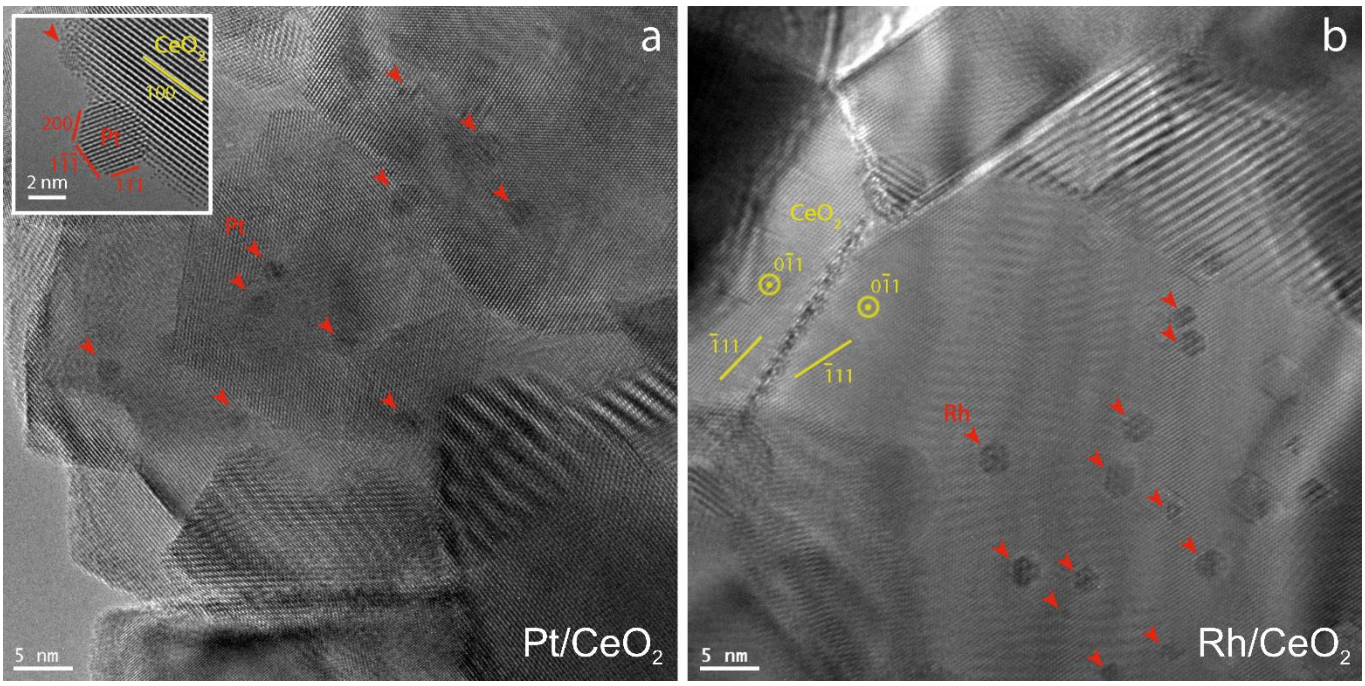

Figure 1. Aberration-corrected TEM images of Pt-CeO_2 (a) and Rh-CeO_2 (b) samples pretreated in H_2 flow at 400 °C. The metal nanoparticles are marked with red arrows. In the insert of (a), the high-resolution image shows a Pt nanoparticle, the facets of which are indexed (red color). In (b), the lattices of two ceria crystallites are indexed (yellow color)

Operando DRIFTS–mass spectrometry measurements

The IR spectrometer used is a Vertex 80v featuring a homebuilt extension with all necessary feedthroughs so that the complete optical path remained evacuated at all times during the experiment. We used a high-temperature reaction chamber (Harrick) fitted with CaF_2 windows and a Praying Mantis diffuse reflection accessory (Harrick). Temperatures were measured by means of a 0.34 mm diameter type K thermocouple placed directly in the catalytic bed, cf.[22, 23] Mass flow controllers and pressure controllers (Bronkhorst) regulated feed and total pressure. Two mass flow regimes were used in the experiments. An O_2-rich feed (relative to the stoichiometry of the reaction) of 1:1 q_{CO}:q_{O_2} (or 4:4 vol%) and a CO-rich feed 7:1 q_{CO}:q_{O_2} (or 7:1 vol%) were used (with q_m denoting the mass flow rate at 50 °C). The total flow was 10.2 mL min^{-1} for all experiments shown here. As an inert gas, He was dosed constantly at 9.4 mL min^{-1} while for the O_2 rich feed the flows for both CO and O_2 were 0.4 mL min^{-1} and for the CO rich feed the flow for CO was 0.7 mL min^{-1} and 0.1 mL min^{-1} for O_2. 10 min elapsed between two cycles under identical feed. Upon switching, the fluxes were allowed to stabilize before the next cycle was started, which usually took around 10 min. After the reactor, a small amount of the exhaust gas stream was split using a fine leak valve to the inlet of a quadrupole mass spectrometer (Hiden Analytical HAL 301) operated at a pressure of $5^{*}10^{-7}$ mbar (base pressure < $2^{*}10^{-10}$ mbar). The total pressure of the reactor system was maintained at 100 mbar using pressure controllers (Bronkhorst). This relatively low pressure is necessary to reduce the response time between exit of the gases from the reactor and their detection by the mass spectrometer. CO (purity 99.997 %) and O_2 (purity 99.999 %) were supplied by Linde. He (purity 99.996 %), CO_2, CO and O_2 were monitored with the QMS. The signals for O_2 and CO evolved consistently with the CO_2 signals. They were not elaborated further and are not shown. The CO_2 signal was normalized to the He signal in order to compensate for effects due to variations in the total pressure at the mass spectrometer level for experiments on

Table 1. Characteristics of the samples

Sample name	Metal loading (wt%)[a]	Metal particle size (nm)[b]	Mean ceria crystallite size / lattice parameter (nm)[c]	Surface area (m^2/g)[d]
CeO_2	0	-	24 / 0.54134	28
Pt-CeO_2	0.98	4.0 ± 1.3	27 / 0.54123	17
Rh-CeO_2	0.73	4.7 ± 1.5	39 / 0.54136	12

[a] Determined by ICP-OES.

[b] Determined by TEM for samples heated to 400 °C in H_2 flow.

[c] Determined by XRD Rietvield refinements for as-prepared catalysts.

[d] Determined by N_2 adsorption volumetry (BET) for as-prepared catalysts

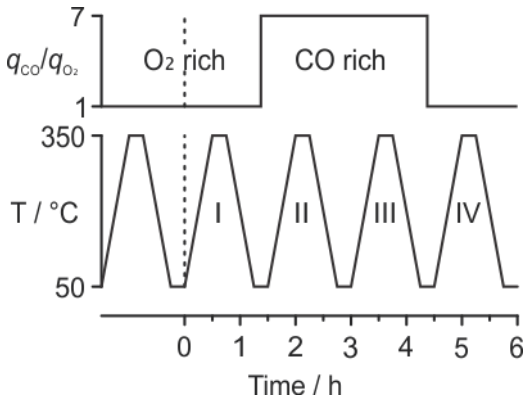

Figure 2. Experimental Protocol

the different powders as well as for drifts in the mass spectrometer sensitivity between the experiments.

A baseline was subtracted to compensate for slightly differing total pressures and improve comparability. The temperature was ramped at 10 °C min^{-1} and the IR spectra acquired at 1 spectrum min^{-1} or equivalently 1 spectrum per 10 °C.

Results and discussion

Catalyst characterization

The samples were analyzed by N_2 adsorption volumetry (BET method), inductively coupled plasma optical emission spectroscopy (ICP-OES), powder X-ray diffraction (XRD), and aberration-corrected transmission electron microscopy (TEM). Figure 1 shows aberration-corrected TEM images of Pt-CeO_2 (a) and Rh-CeO_2 (b) samples pretreated in H_2 flow at 400 °C. The samples present CeO_2 grains separated by straight boundaries. They are arranged as in a puzzle, which is characteristic of ceria materials synthesized by solution combustion.[8,10] Metal nanoparticles are clearly visible in both samples. Imaging of metal particles anchored at the edges of ceria grains shows well-faceted fcc particle morphologies (insert in a). The main characteristics of the samples are shown in Table 1. As determined from XRD measurements, the SCS-prepared materials exhibit the fluorite structure of standard CeO_2 (space group Fm-3m, #225).[8] The BET specific surface areas are in the 12–28 m^2g^{-1} range, which corresponds to 39-24 nm in terms of ceria crystallite sizes. The metal loadings are 0.98 wt% for Pt-CeO_2 and 0.73 wt% for Rh-CeO_2, and the mean metal particle size is 4–5 nm. As shown in previous investigations using electron microscopies, the samples exhibit a sponge-like microstructure with round macropores, irrespective of the metal presence or nature.[8, 10,18]

Experimental Protocol

Figure 2 schematically depicts the experimental procedure. After synthesis, the powders can be assumed to be partially oxidized and may contain residuals from the synthesis. In order to clean the powders and establish a well-defined initial state, the powders were first exposed to an O_2-rich feed (relative to the stoichiometry of the reaction) at 50 °C. The temperature of the sample was then ramped from 50 to 350 °C at 10 °C min^{-1}, kept constant at 350 °C for 10 min, and cooled back to 50 °C at 10 °C min^{-1}. This oxidative cycle burns preparation residuals and oxidizes the powders. The beginning of the next cycle corresponds to the experimental t_0: an IR reference is taken and the QMS data are recorded. The experiment then consists of 4 cycles where the temperature is ramped using the parameters given above. Cycle I uses an O_2-rich feed. It is followed by two cycles (Cycle II and Cycle III) with a CO-rich feed. Cycle IV is under O_2-rich feed again (same conditions as Cycle I).

The four cycles therefore represent four different feed/surface state conditions:

Cycle I exposes an *oxidized* catalyst to an O_2 rich (*oxidizing*) feed;

Cycle II exposes an *oxidized* catalyst to a CO rich (*reducing*) feed;

Cycle III is, therefore, assumed to start on a reduced catalyst and, thus, exposes a *reduced* catalyst to a *reducing* feed; and

Cycle IV exposes a *reduced* catalyst to an *oxidizing* feed.

Reactivity study, mass spectrometry

Figure 3 shows the CO_2 signal recorded during the oxidation of CO on pure ceria, Rh-ceria, and Pt-ceria prepared by SCS. On CeO_2, no significant CO_2 production (considering 5 % of the signal at saturation as significant) was detected below 200 °C. At higher temperatures CO_2 production increases linearly with the temperature until it levels out at 350 °C. Nearly twice as much CO_2 is produced under O_2-rich conditions (Cycle I) as compared to CO-rich conditions (Cycle II and Cycle III). This result is consistent with the experimental conditions. Indeed, under O_2-rich conditions (excess of O_2 with respect to the stoichiometry) we provide ½ mole of CO per ½ mole of O_2, and can therefore expect ½ moles of CO_2 to be produced. In contrast, under CO-rich conditions, we provide $^7/_8$ mole of CO per $^1/_8$ mole of O_2, yielding 2 × $^1/_8$ = ¼ mole of CO_2 being produced at total consumption of O_2, or half the CO_2 production under O_2-rich conditions. Pure CeO_2 catalyzes CO_2 production[1, 24], hence this first experiment demonstrates that the simple one-pot SCS preparation method is suitable for preparing catalytically active ceria powders. The fourth heating and cooling cycle for this sample has been omitted for technical reasons. It did not show major differences to the behavior of the previous cycles featuring O_2 excess.

Figure 3b shows that the presence of Rh leads to a decrease in the onset temperature of CO_2 formation to 160 °C. Total conversion is observed at 210 °C under CO-rich conditions and at 240 °C under O_2-rich conditions. Saturation is therefore reached earlier than with pure CeO_2. Notwithstanding the absolute CO_2 saturation value, the four cycles are similar.

Figure 3c, Pt-CeO_2 exhibits a peculiar behavior with regard to CO_2 production that requires a detailed discussion. Cycle I shows the onset of CO_2 production at 170 °C until saturation is reached at 295 °C. Upon cooling we observe a similar behavior. For Cycle II under CO-rich conditions, the heating ramp again shows a similar behavior albeit with half of the CO_2

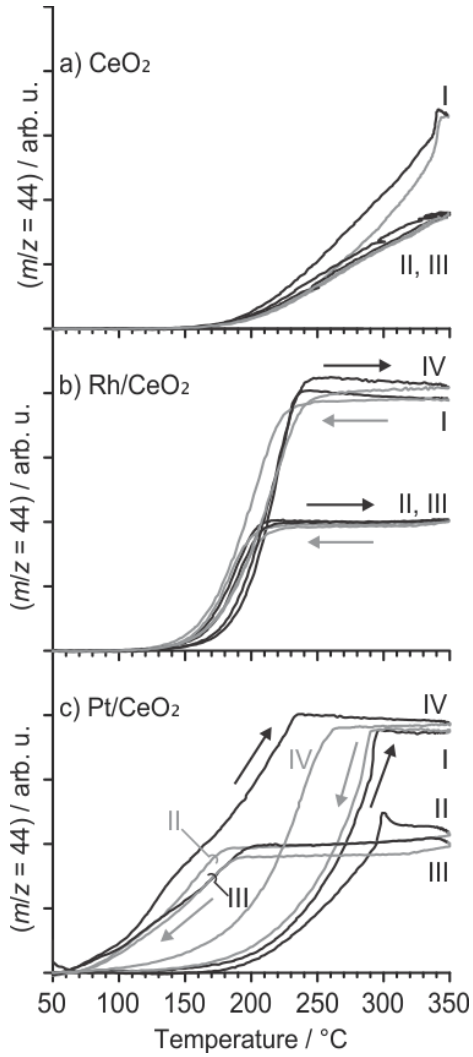

Figure 3 CO_2 signal measured as a function of the temperature during CO oxidation on a) pure CeO_2; b) Rh-CeO_2; c) Pt-CeO_2. Heating ramps are drawn in black and cooling ramps in gray. Note that the *y*-scale (arbitrary units) is the same for all three graphs

production, as expected. During the following cooling, however, CO_2 production remains at the saturation value down to 180 °C. CO_2 production then decreases slowly but CO_2 is still detected at temperatures as low as 85 °C. For Cycle III, under CO-rich conditions, the latter behavior is reproduced: Onset temperature appears at about 85 °C and saturation occurs at 180 °C. Cycle IV, the last cycle under O_2-rich conditions, shows an onset at 70 °C and saturation at 235 °C. The final cooling shows a behavior that is in between those observed for the heating ramps of Cycle IV and Cycle I.

The heating and cooling in Cycle I and Cycle III do not show significant differences between heating and cooling, whereas large differences appear when the reaction conditions change (Cycle II and Cycle IV). Unlike for CeO_2 and Rh-CeO_2, CO_2 production is detected at remarkably low temperatures for the reaction running under reducing conditions. CO_2 production was reported at 52 °C on Pd-CeO_2 powders reduced by H_2.[25] So we postulate that the oxidation state of the support plays a role in the change of activity. In order to confirm this result and study the surface state more precisely, the next section discusses the IR spectroscopic results acquired during these experiments.

The catalysts were also tested in a conventional flow fixed bed reactor, using slow temperature cycles (1.33 °C/min) and 2% CO : 2% O_2 conditions (i.e., close to the present "O_2-rich" conditions, 4% CO : 4% O_2).[8] The two sets of results are consistent with each other, showing the same hierarchy of activities (see Figure 3, cycles I).

Monitoring the Surface state by Operando DRIFTS

CeO_2

Figure 4 shows the spectra acquired during Cycle I and Cycle II (top) as well as the last spectrum of each cycle taken at 50 °C (bottom). Cycle III was similar to Cycle II and Cycle IV similar to Cycle I. They are therefore not plotted. Every spectrum is referenced to t_0 according to our protocol. The first spectrum of Cycle I, being the reference, is flat and the features observed thereafter are changes in absorbance with regard to this initial state. The large asymmetric feature at 2300–2400 cm^{-1} corresponds to the CO_2 gas phase signal and the feature at 2050–2220 cm^{-1} corresponds to gas phase CO. As expected, the gas phase CO_2 signal becomes stronger (i.e. more negative or more absorption) with higher temperatures as the CO signal becomes more positive, which corresponds to a loss of intensity with regard to the reference. This is consistent with the mass spectrometry data presented above and the gas phase signals are not discussed further.

Above 100 °C, several bands develop in the carbonate and carboxylate region at 1000–1700 cm^{-1}. Note that an exhaustive description of this region is generally difficult as literature offers varying assignments for some features[26-29] and is beyond the scope of this article. We instead focus on the features most apparent in our spectra. The intense 1530–1660 cm^{-1} region is mostly attributed to a carbonate stretching mode.[30] The second most intense band at 1300 cm^{-1} (green) could originate from bridged and bidentate carbonate species.[31] The parallel development of the bands at 1028, 1300 and 1564 cm^{-1} may suggest that these bands are caused by the same species. The band structure in the 1260–1450 cm^{-1} region is more complex at higher temperatures where the band at 1400 cm^{-1} and the two sharp bands at 1372 and 1358 cm^{-1} (orange)with a shoulder at 1365 cm^{-1} can be related to polydentate carbonates[27] or possibly formates.[29, 31] A negative band is visible at 1446 cm^{-1} above 90–100 °C (grey) and its intensity further increases with the temperature. We attribute it to the formation of polydentate carbonates from the presence of CO_2.[24, 28]

Positive bands indicate that the monodentate carbonates are lost upon heating above 90–100 °C and the polydentate carbonates band seems to saturate near 180 °C. This temperature corresponds to the onset of CO_2 production measured by mass spectrometry and could, therefore, indicate that the polydentate carbonates play a role in the reaction mechanism. This is also consistent with the increase of the negative band at 1446 cm^{-1} (grey) (indicating formation of a new species) attributed to reaction of adsorbed CO_2.

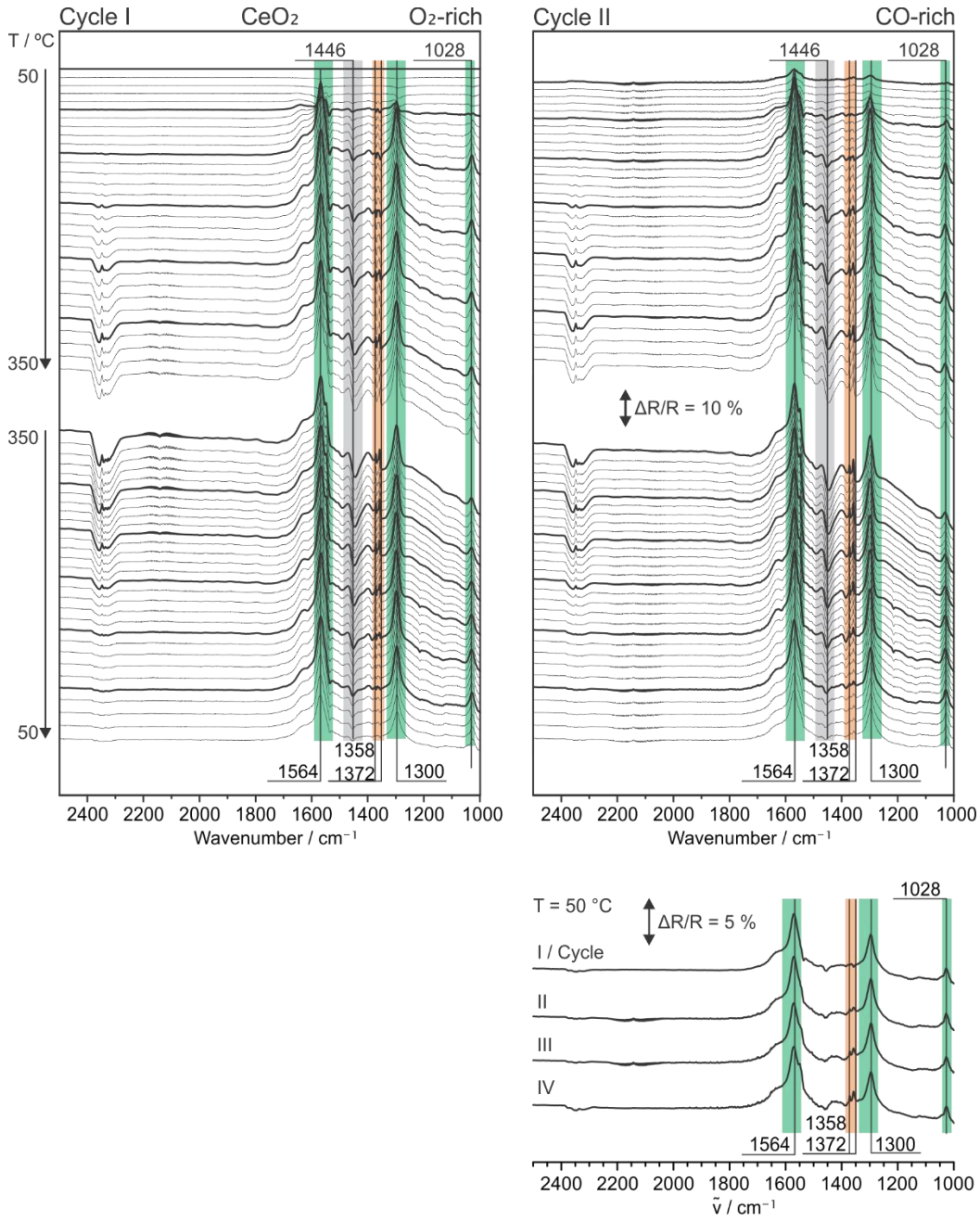

Figure 4. DRIFTS measurements taken during the temperature ramps from 50 to 350 °C and back under O_2-rich conditions (Cycle I) and CO-rich conditions (Cycles II) on pristine CeO_2. The waterfall plots show temperature dependent series during selected cycles and the bottom plots display the last spectrum (measured at 50°C) for each cycle

Interestingly, the positive bands are present down to 50 °C upon cooling but are mostly gone at the beginning of next cycle under CO-rich conditions, that is after over 10 min at 50 °C. Therefore, the carbonates are removed during the O_2-rich cycle and are formed after the replacement of the O_2-rich by the CO-rich flow. The formation of carbonates and formates therefore appears to be mostly reversible. This further indicates that the bands observed are not residuals from the preparation but indeed species adsorbed at the CeO_2 surface. Comparison of the spectra at 50 °C (bottom part of the figure) shows small changes after each cycle. The bands attributed to polydentate carbonates or formates at 1372 and 1365–1358 cm^{-1} (orange) become increasingly prominent at room temperature. This could indicate further cleaning of the surface during the reaction cycles but no stronger modification of the powders.

No major changes can be observed between the results for Cycles I and Cycle II. This agrees well with previous studies, see e.g. [31].

Overall, some of the carbonaceous species disappear at least partially as the temperature increases and form again as the temperature decreases, except for the species associated with the band at 1446 cm^{-1} (grey), which shows the reverse behavior.

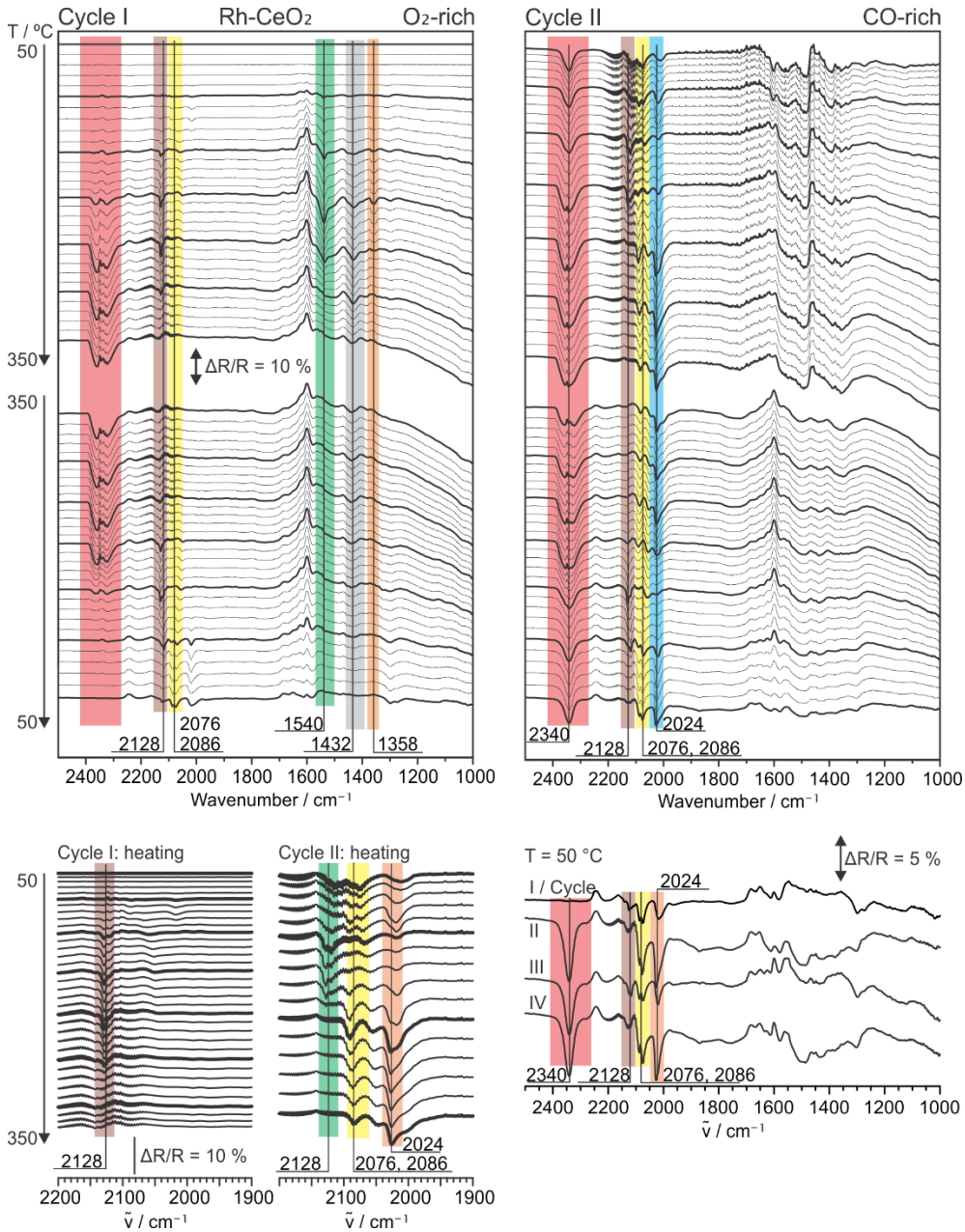

Figure 5. DRIFTS measurements taken during the temperature ramps from 50 to 350 °C and back under O_2-rich conditions (Cycle I) and CO-rich conditions (Cycles II) on Rh-CeO_2. The waterfall plots show temperature dependent series during selected cycles; the bottom left plots show a zoom on the CO region during the heating period of the first two cycles (for cycle II every second spectrum has been omitted for clarity); the bottom right plots display the last spectrum (measured at 50°C) for each cycle.

Rh-CeO_2

Figure 5 displays the DRIFTS measurements for Rh-CeO_2. Under O_2-rich feed, the monodentate region (1532–1660 cm^{-1}) displays an envelope comparable to the one discussed for CeO_2 but with signal intensities that are lower by approximately a factor of two. The polydentate carbonates and formates corresponding to wavenumbers lower than 1450 cm^{-1} are not clearly visible. Instead three negative bands develop in this region above 100 °C. The sharp negative band at 1540 cm^{-1} (green) and two broader bands at 1432 (grey) and 1358 cm^{-1} (orange) then lose intensity above 300 – 310 °C and the band at 1540 cm^{-1} is not visible anymore at 350 °C. From the positions and the temperatures, they are assigned to bound CO_2.[28] We further assume that the carbonates (and possibly carboxylates) formed desorb above 310 °C.

Under CO-rich feed, an extra negative band (new species) is observed at 2340 cm^{-1} at 50 °C (red). The band appears upon changing the composition of the feed. This wavenumber would correspond to gas phase CO_2. [32] The band shape, however, does not feature the usual nodal plane and is, therefore, attributed to CO_2 located at sites where rotations are frustrated, most likely in the smallest pores of the powders. The band overlaps with the gas phase CO_2 signal so that it is difficult to discuss its evolution with temperature. Nevertheless, the envelope of the CO_2 signal at 350 °C does not seem to be largely changed upon comparison with the experiments on CeO_2. The region of carbonaceous species

caused by CO and CO_2 adsorption now shows a more complex structure than under O_2-rich feed with negative bands (new species) below 1450 cm^{-1}. The envelope of the carbonate band further changes between 50 °C and 130 °C. Carbonates were observed on pure CeO_2 but are only present under CO-rich feed and to a lower extent on Rh-ceria, which suggests that Rh catalyzes CO oxidation and carbonate formation. We can now discuss the Rh–CO region in the 1950–2150 cm^{-1} range. Upon heating in the O_2-rich feed, a band at 2128 cm^{-1} (brown) with a shoulder at 2122 cm^{-1} is clearly resolved for temperatures between 140 °C and 300 °C. These wavenumbers are above the CO atop region. The features are not observed anymore above 300 °C. *Gem*-dicarbonyl $Rh(CO)_2$ species, indicating the presence of highly dispersed Rh have been observed for wavenumbers up to 2117 cm^{-1}.[8,33-35] However, such species present coupled vibration modes generating two distinct IR bands.

Coadsorption of oxygen and CO on a Rh(111) surface also leads to a shift of the CO-Rh atop peaks to higher wavenumbers.[33, 36-38] The activity reported in Figure 3b is similar under oxidative or reductive flux so that we rule out the presence of rhodium oxide proposed in[39-41] but not observed in other studies[33, 37, 38]. Upon cooling in the O_2-rich feed, a double negative absorption band at 2076 and 2086 cm^{-1} (yellow) is now identified. It can be attributed to dense phase of atop CO onto Rh terraces.[36, 42] The other peak at 2024 cm^{-1} (orange) could correspond to less dense packing[36, 42], probably on smaller and more defective particles. The appearance of these new features may well indicate sintering and faceting of some Rh particles at the ceria surface.

The CO-rich feed shows three different regimes upon heating and cooling as well. The CO features at 2086, 2076, and 2024 cm^{-1} attributed to CO atop are visible at low temperature. Between 100 and 200 °C, these features lose intensity and two bands appear at 2128 and 2118 cm^{-1}. These bands are better resolved during cooling. At higher temperatures, the new bands vanish and the spectra are more similar to the low temperature ones. The temperature range where the 2128/2118 cm^{-1} bands disappear corresponds to the onset of the reaction as measured using the mass spectrometer. We, therefore, tentatively attribute the features to a dense phase with coadsorbed oxygen and CO. Once oxygen and CO are already present at the Rh surface, the reaction proceeds quickly as soon as the temperature is high enough to overcome the activation barrier. This fits very well with the activity measurements reported in Figure 3b where the CO_2 formation rate went from zero to saturation within a range of 50 °C, in strong contrast to the 300 °C range observed on pure CeO_2. At higher temperatures, corresponding to the region of maximum reaction rate in Figure 3b, oxygen (the limiting reactant under CO rich flux) is efficiently reacted to CO2 and its residence time at the surface becomes very small.

Table 2: Assignment of observed IR bands on different catalyst powders

Sample	Wavenumber [cm^{-1}]	Assignment	Reference
CeO_2	1564	bidentate carbonate	26, 28, 31
		formate	29
	1446	polydentate carbonate	24, 26, 28, 29, 31
	1358, 1372	polydentate carbonate	26, 28, 31
		formate species	29
	1300	bidentate carbonate	26, 28, 29, 31
	1028	bidentate carbonate	4, 26, 28, 29
Rh-CeO_2	2128	densely packed CO coadsorbed with O	33, 36-38
	2076, 2086	densely packed CO atop Rh terraces	36, 42
	2024	CO atop Rh terraces	36, 42
	1540, 1432, 1358	carbonaceous species	28, 31
Pt-CeO_2	2118	CO on Pt coadsorbed w/ high oxygen coverage or on Pt(II)	32, 43, 44
	2106	CO on Pt coadsorbed w/ oxygen	32, 43, 44
	2076, 2090	CO atop Pt steps and edges	45-47
	2098	CO on Pt coadsorbed w/ oxygen	32, 43, 44
	1574	bidentate carbonate	26, 31
		formate	29
	1446	polydentate carbonate	26, 29, 31
	1350, 1372	polydentate carbonate	26, 28, 29
		formate	29
	1296	bidentate carbonate	26, 28, 29
	1029	bidentate carbonate	26, 28, 29

Consequently, the spectra therefore revert back to CO/Rh case.

In summary, the influence of Rh can be summarized as follows. The classical explanation implies that the light off starts when the temperature is sufficiently high to allow for CO desorption. Under these conditions dissociative adsorption of oxygen becomes possible and the LH mechanism on Rh is sustained. In addition to this, further reaction channels are identified. Especially under O_2-rich conditions, Rh effectively catalyzes CO oxidation to carbonates. Formation of these carbonaceous species, which reside on the ceria constitute an additional CO oxidation channel. Ceria provides additional oxygen for this channel through activation at defects (Mars-van-Krevelen mechanism) and reverse spillover. The latter is indicated by the coadsorption features observed at high wavenumbers in the CO region for CO adsorption on Rh.

Pt-CeO_2

Figure 6 and Figure 7 show the development of the spectra for Pt-CeO_2. The carbonaceous species region 1000–1700 cm^{-1} displays essentially the same features than observed on pure CeO_2 with a more intense positive difference band (removed species) at 1598 cm^{-1} (green). On the other side of the spectral window, the band at 2340 cm^{-1} is observed for Pt-CeO_2 as well as Rh-CeO_2 (red) but not for pure CeO_2 after the first CO-rich cycle. Even though we still cannot precisely assign it, it is apparently related to the presence of the metal particles. Explanations for the interesting behavior reported in Figure 3c must therefore be sought in relation to the CO–Pt region at 2130–1900 cm^{-1} (yellow). During Cycle I, a small negative absorption band appears at 2112 cm^{-1} at 70–80 °C and shifts to 2118 cm^{-1} at 180 °C and above. It loses intensity above 250 °C. At the same time, a positive absorption band appears at 2094 cm^{-1}, shifts to 2098 cm^{-1} at 180 °C, and to 2104 cm^{-1} at 350 °C. Upon cooling to 50 °C, the spectra is nearly flat again, which indicates that the surface is close to its state at t_0. Stronger changes occur during Cycle II and Cycle III (CO-rich). After the CO-rich cycles, Pt features a positive band (decreased signal) at 2106 cm^{-1} and negative bands at 2090 and 2076 cm^{-1}. The changes are conserved at 50 °C as the spectra show no change during the 10 minute resting period. This is a clear indication that the Pt surface is modified by the CO-rich flux. CO adsorbs atop at Pt steps with a strong IR absorption at about 2090 cm^{-1}.[45-47] CO atop Pt nanoparticle edges appears as a shoulder at about 2070 cm^{-1}.[45] Coadsorption with O_2 typically gives rise to a shift of the bands to higher wavenumbers to about 2110 cm^{-1}.[32] Alternatively, bands at 2110 cm^{-1} and above have also been assigned to CO adsorbed on Pt(II)O particles. [43, 44] Platinum oxide, however, was shown to be less active than metallic Pt under the present conditions.[48, 49] Comparing with our spectra, the features observed after the CO-rich cycles (Cycle II and Cycle III) are therefore assigned to CO/Pt(0). The features observed during the O_2-rich cycles (Cycle I and Cycle IV) correspond to O and CO coadsorption, possibly involving partial oxidation of the particles. As discussed above, this change of the Pt particles is

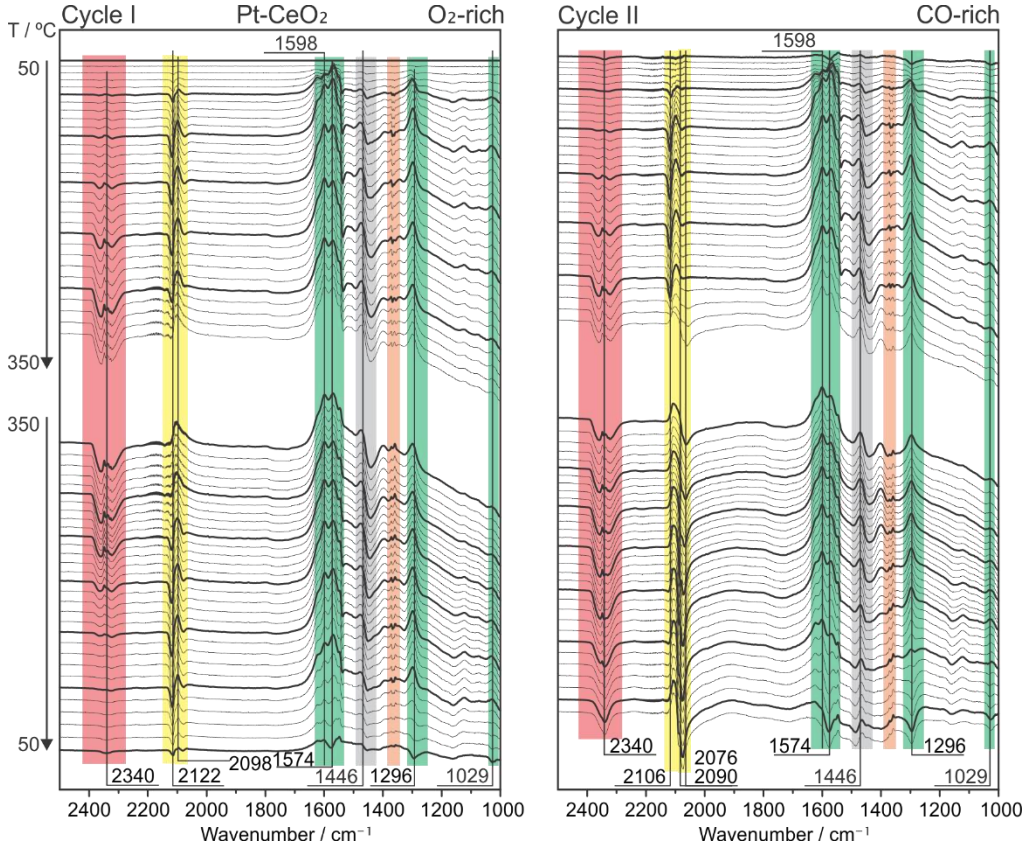

Figure 6. DRIFTS measurements taken during the temperature ramps from 50 to 350 ºC and back under O_2-rich conditions (cycle I) and CO-rich conditions (cycle II) on Pt-CeO_2

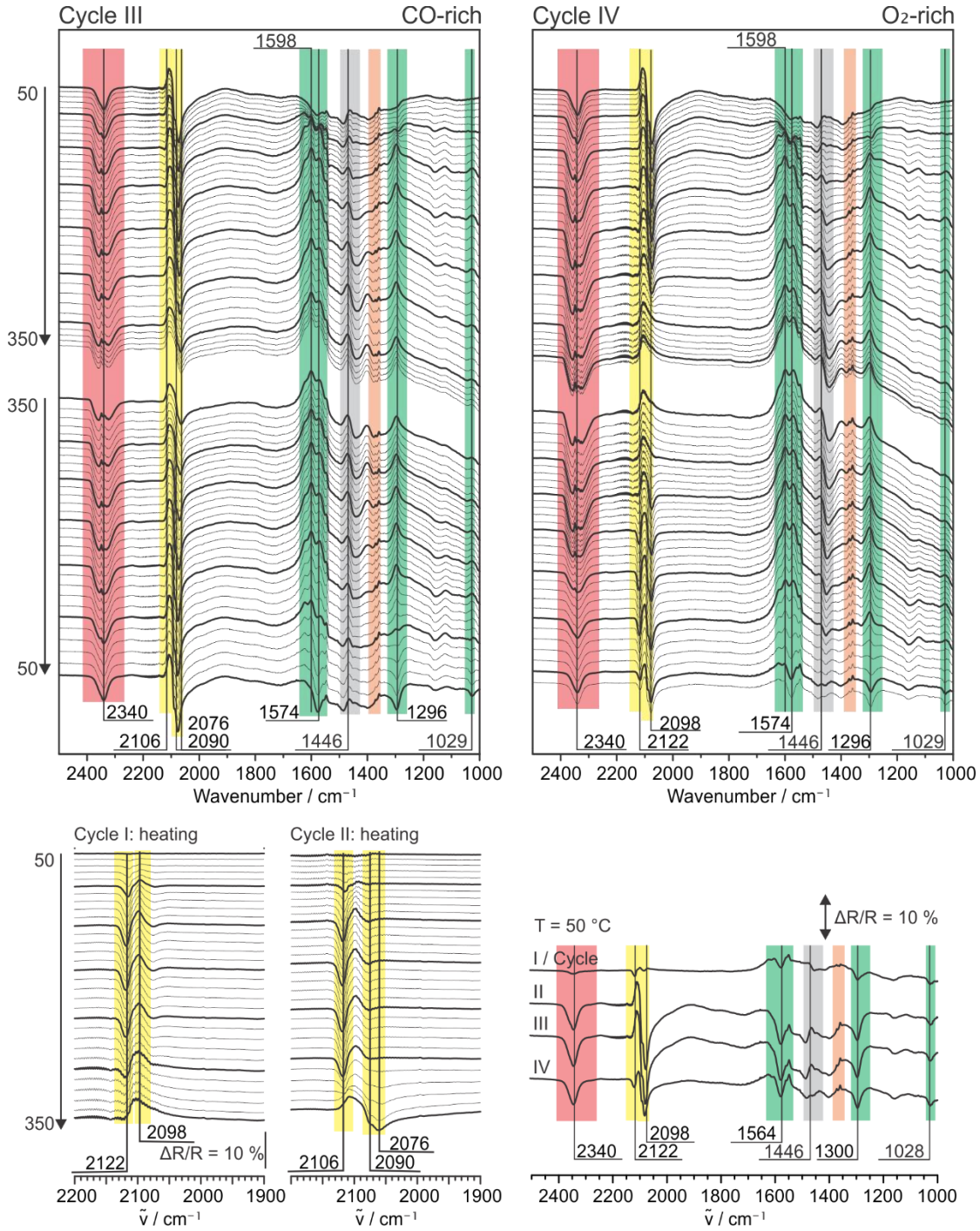

Figure 7. DRIFTS measurements taken during the temperature ramps from 50 to 350 °C and back under O_2-rich conditions (cycle IV) and CO-rich conditions (cycle III) on Pt-CeO_2. The waterfall plots show temperature dependent series during the cycles; the bottom left plots show a zoom on the CO region during the heating of the first two cycles; the bottom right plots display the last spectrum (measured at 50°C) for each cycle

responsible for the different rates of CO oxidation observed in Figure 3c. We also note that the change of regime observed in Cycle II and Cycle IV is a relatively slow process. This allows us to conclude that Pt is partially oxidized during the O_2-rich cycles and reduced during the CO-rich cycles, leading to the low temperature activity under CO-rich conditions. Pt oxides being hardly stable, we attribute this result to a metal-ceria interaction effect. CO-DRIFTS experiments on the same catalyst already suggested the presence of Pt oxide.[8] The present study further demonstrates that Pt interacts more efficiently with ceria than Rh.

Conclusion

Using a combination of operando DRIFTS spectroscopy and mass spectrometry, we have studied the surface species and activity of pure ceria, Rh-ceria, and Pt-ceria powders for CO oxidation under O_2-rich and CO-rich conditions. The powders

were prepared by one-step, one-pot solution combustion synthesis.

We find that carbonaceous species adsorbed onto the ceria at low temperature are partially removed in the course of the reaction both on pure ceria and on Pt-ceria. For Rh-ceria, the carbonaceous species play a lesser role in the reaction mechanism.

On Rh-ceria, we find that the reaction must overcome two reaction barriers. At 100 °C, oxygen diffuses from the ceria to the rhodium, forming a densely packed O-CO phase. Then, the reaction starts and rapidly reaches maximum activity.

On Pt-ceria, strong interaction with the ceria supports under oxidative conditions leads to partial oxidation of the Pt particles, leading to catalytic performances that are only slightly better than pure ceria in the initial stage. The surface can be reduced under excess CO feed, however, and as a result high activity is obtained down to much lower temperatures, i.e. with an onset below 100 °C.

Acknowledgements

This project was financially supported by the ''Deutsche Forschungsgemeinschaft'' (DFG) within the Excellence Cluster ''Engineering of Advanced Materials'' in the framework of the excellence initiative and within the Research Unit FOR 1878 "funCOS". We acknowledge additional support by the European COST Action CM1104 "Reducible oxide chemistry, structure and functions" by the European Commission and "chipCAT", FP7-NMP-2012-SMALL-6, Grant Agreement no. 310191. Thanh-Son Nguyen and Laurent Piccolo acknowledge the support by the French National Research Agency through the ANR-BS10-009 DINAMIC project.

References

1. A. Trovarelli and P. Fornasiero, *Catalysis by ceria and related materials*, Imperial College Press London, 2002.
2. J. Paier, C. Penschke and J. Sauer, *Chemical reviews*, 2013, **113**, 3949-3985.
3. C. T. Campbell and C. H. F. Peden, *Science*, 2005, **309**, 713-714.
4. E. Aneggi, J. Llorca, M. Boaro and A. Trovarelli, *Journal of Catalysis*, 2005, **234**, 88-95.
5. N. Bion, F. Epron, M. Moreno, F. Mariño and D. Duprez, *Topics in Catalysis*, 2008, **51**, 76-88.
6. E. D. Park, D. Lee and H. C. Lee, *Catalysis Today*, 2009, **139**, 280-290.
7. K. Liu, A. Wang and T. Zhang, *ACS Catalysis*, 2012, **2**, 1165-1178.
8. T.-S. Nguyen, F. Morfin, M. Aouine, F. Bosselet, J.-L. Rousset and L. Piccolo, *Catalysis Today*, 2015, DOI: 10.1016/j.cattod.2014.12.038.
9. M. S. Hegde, G. Madras and K. C. Patil, *Accounts of chemical research*, 2009, **42**, 704-712.
10. T.-S. Nguyen, G. Postole, S. Loridant, F. Bosselet, L. Burel, M. Aouine, L. Massin, P. Gélin, F. Morfin and L. Piccolo, *Journal of Materials Chemistry A*, 2014, **2**, 19822-19832.
11. S. L. González-Cortés and F. E. Imbert, *Applied Catalysis A: General*, 2013, **452**, 117-131.
12. W. Shan, Z. Feng, Z. Li, J. Zhang, W. Shen and C. Li, *Journal of catalysis*, 2004, **228**, 206-217.
13. J. Papavasiliou, G. Avgouropoulos and T. Ioannides, *Applied Catalysis B: Environmental*, 2006, **66**, 168-174.
14. P. Yaseneva, S. Pavlova, V. Sadykov, E. Moroz, E. Burgina, L. Dovlitova, V. Rogov, S. Badmaev, S. Belochapkin and J. Ross, *Catalysis Today*, 2008, **138**, 175-182.
15. V. M. Gonzalez-Delacruz, F. Ternero, R. Pereñíguez, A. Caballero and J. P. Holgado, *Applied Catalysis A: General*, 2010, **384**, 1-9.
16. L. Pino, A. Vita, F. Cipitì, M. Laganà and V. Recupero, *Applied Catalysis B: Environmental*, 2011, **104**, 64-73.
17. D. H. Prasad, S. Y. Park, H. Ji, H.-R. Kim, J.-W. Son, B.-K. Kim, H.-W. Lee and J.-H. Lee, *Applied Catalysis A: General*, 2012, **411**, 160-169.
18. G. Postole, T.-S. Nguyen, M. Aouine, P. Gélin, L. Cardenas and L. Piccolo, *Applied Catalysis B: Environmental*, 2015, **166**, 580-591.
19. S. R. Jain, K. C. Adiga and V. R. P. Verneker, *Combustion and flame*, 1981, **40**, 71-79.
20. L. Kępiński and J. Okal, *Journal of Catalysis*, 2000, **192**, 48-53.
21. A. Badri, C. Binet and J.-C. Lavalley, *The Journal of Physical Chemistry*, 1996, **100**, 8363-8368.
22. H. Li, M. Rivallan, F. Thibault-Starzyk, A. Travert and F. C. Meunier, *Physical Chemistry Chemical Physics*, 2013, **15**, 7321-7327.
23. T. Bánsági, T. S. Zakar and F. Solymosi, *Applied Catalysis B: Environmental*, 2006, **66**, 147-150.
24. A. Trovarelli, *Catalysis Reviews*, 1996, **38**, 439-520.
25. M. Jin, J.-N. Park, J. Shon, Z. Li, M. Yoon, H. Na, Y.-K. Park and J. Kim, *Res Chem Intermed*, 2011, **37**, 1181-1192.
26. C. Li, Y. Sakata, T. Arai, K. Domen, K.-i. Maruya and T. Onishi, *Journal of the Chemical Society, Faraday Transactions 1: Physical Chemistry in Condensed Phases*, 1989, **85**, 929-943.
27. C. Mondelli, V. Dal Santo, A. Trovarelli, M. Boaro, A. Fusi, R. Psaro and S. Recchia, *Catalysis today*, 2006, **113**, 81-86.
28. C. Binet, M. Daturi and J.-C. Lavalley, *Catalysis Today*, 1999, **50**, 207-225.
29. G. N. Vayssilov, M. Mihaylov, P. S. Petkov, K. I. Hadjiivanov and K. M. Neyman, *The Journal of Physical Chemistry C*, 2011, **115**, 23435-23454.
30. A. M. Turek, I. E. Wachs and E. DeCanio, *The Journal of Physical Chemistry*, 1992, **96**, 5000-5007.
31. C. Binet, A. Badri, M. Boutonnet-Kizling and J.-C. Lavalley, *J. Chem. Soc., Faraday Trans.*, 1994, **90**, 1023-1028.
32. J. D. Krooswyk, J. Yin, A. L. Asunskis, X. Hu and M. Trenary, *Chemical Physics Letters*, 2014, **593**, 204-208.
33. S. M. McClure and D. W. Goodman, *Chemical Physics Letters*, 2009, **469**, 1-13.
34. M. Frank, R. Kühnemuth, M. Bäumer and H.-J. Freund, *Surface science*, 2000, **454**, 968-973.
35. J. Evans, B. Hayden, F. Mosselmans and A. Murray, *Surface Science Letters*, 1992, **279**, L159-L164.

36. G. Krenn, I. Bako and R. Schennach, *The Journal of chemical physics*, 2006, **124**, 144703.
37. M. S. Chen, Y. Cai, Z. Yan, K. K. Gath, S. Axnanda and D. W. Goodman, *Surface Science*, 2007, **601**, 5326-5331.
38. F. Gao, Y. Cai, K. Gath, Y. Wang, M. Chen, Q. Guo and D. Goodman, *The Journal of Physical Chemistry C*, 2008, **113**, 182-192.
39. J. Gustafson, R. Westerstrom, O. Balmes, A. Resta, R. Van Rijn, X. Torrelles, C. Herbschleb, J. Frenken and E. Lundgren, *The Journal of Physical Chemistry C*, 2010, **114**, 4580-4583.
40. J. Gustafson, R. Westerström, A. Mikkelsen, X. Torrelles, O. Balmes, N. Bovet, J. N. Andersen, C. J. Baddeley and E. Lundgren, *Physical Review B*, 2008, **78**, 045423.
41. J. Gustafson, R. Westerström, A. Resta, A. Mikkelsen, J. N. Andersen, O. Balmes, X. Torrelles, M. Schmid, P. Varga and B. Hammer, *Catalysis Today*, 2009, **145**, 227-235.
42. H. P. Koch, P. Singnurkar, R. Schennach, A. Stroppa and F. Mittendorfer, *The Journal of Physical Chemistry C*, 2008, **112**, 806-812.
43. M. Primet, J. M. Basset, M. V. Mathieu and M. Prettre, *Journal of Catalysis*, 1973, **29**, 213-223.
44. P.-A. Carlsson, L. Österlund, P. Thormählen, A. Palmqvist, E. Fridell, J. Jansson and M. Skoglundh, *Journal of Catalysis*, 2004, **226**, 422-434.
45. J. Xu and J. T. Yates, *Surface science*, 1995, **327**, 193-201.
46. B. E. Heyden and A. M. Bradshaw, *Surface Science*, 1983, **125**, 787-802.
47. M. Primet, *Journal of Catalysis*, 1984, **88**, 273-282.
48. M. Chen, Y. Zheng and H. Wan, *Topics in Catalysis*, 2013, **56**, 1299-1313.
49. A. L. Gerrard and J. F. Weaver, *The Journal of chemical physics*, 2005, **123**, 224703.